J. Fluid Mech. (2021), *vol*. 915, R5, doi:10.1017/jfm.2021.226

Thermal boundary-layer structure in laminar horizontal convection

Bo Yan[1], **Olga Shishkina**[2] **and Xiaozhou He**[1,2,†]

[1]School of Mechanical Engineering and Automation, Harbin Institute of Technology, Shenzhen, 518055 China

[2]Max Planck Institute for Dynamics and Self-Organization (MPIDS), 37077 Göttingen, Germany

(Received 12 February 2021; revised 4 March 2021; accepted 6 March 2021)

We present experimentally obtained time-averaged vertical temperature profiles $\theta(z)$ in horizontal convection (HC) in water (Prandtl number $Pr \simeq 6$), which were measured near the heating and cooling plates that are embedded in the bottom of HC samples. Three HC rectangular samples of different sizes but the same aspect ratio $\Gamma \equiv L : W : H = 10 : 1 : 1$ (L, W and H are the length, width and height of the sample, respectively) were used in the experiments, which allowed us to study HC in a Rayleigh-number range $2 \times 10^{10} \lesssim Ra \lesssim 9 \times 10^{12}$. The measurements revealed that above the cooling plate, the mean temperature profiles have a universal scaling form $\theta(z/\lambda_c)$ with λ_c being a Ra-dependent thickness of the cold thermal boundary layer (BL). The $\theta(z/\lambda_c)$-profiles agree well with solutions to a laminar BL equation in HC, which is derived under assumption that the large-scale horizontal velocity achieves its maximum near the plate and vanishes in the bulk. Above the heating plate, the mean temperature field has a double-layer structure: in the lower layer, the θ profiles scale with the hot thermal BL thickness λ_h, while in the upper layer, they again scale with λ_c. Both scaling forms are in good agreement with the solutions to the BL equation with a proper parameter choice.

Key words: boundary layer structure

1. Introduction

Boundary layer (BL) has a great impact in wall-bounded thermal convection. It affects global heat and momentum transport through the thermally driven flow, and influences the mixing processes of mass and heat in the fluid. The thermal BL structure is probably best studied in Rayleigh–Bénard convection (RBC), which occurs in a fluid layer heated from below and cooled from above (Ahlers, Grossmann & Lohse 2009). Slightly above the onset of convection, when the thermal driving (expressed by the Rayleigh number

† Email address for correspondence: hexiaozhou@hit.edu.cn

Ra) is relatively weak, the convective flow is laminar and therefore laminar Prandtl BL equations with appropriate choice of the boundary conditions can approximate well the temperature profiles (Schlichting & Gersten 2000). On the other side, when *Ra* is extremely high, the turbulent interior flow renders the BL fully turbulent. In this case, the BL structure is predicted to follow the logarithmic dependence on the distance from the boundaries (Kraichnan 1962; Spiegel 1971; Shraiman & Siggia 1990; Grossmann & Lohse 2011). In many practical RBC flows of interests, however, *Ra* is between the two extreme cases and the BL structure is more complicated. For this case, in Shishkina *et al.* (2015), Shishkina *et al.* (2017), Ching, Dung & Shishkina (2017) and Ching *et al.* (2019), equations for the temperature BL were derived that take into account turbulent fluctuations in terms of the eddy viscosity and eddy thermal diffusivity and also the fact that the mean horizontal velocity (wind) has a single maximum, while vanishing at the plate and deep in the bulk. This differs the BL equations for RBC from the Prandtl–Blasius–Pohlhausen (PBP) equations that describe a laminar BL above a horizontal plate which is blown by a constant wind. Analogously, equations for the temperature variance profiles were derived for $Pr \gtrsim 1$ (Wang, He & Tong 2016; Wang *et al.* 2018) and $Pr \lesssim 1$ (He, Bodenschatz & Ahlers 2021; Xu *et al.* 2021). One should note that although the shape of the temperature profiles in RBC differs from the PBP ones, the BLs in RBC and in a PBP flow are similar scaling wise. In particular, in both cases, the mean heat transport, represented by the Nusselt number *Nu*, scales as a square root of the Reynolds number *Re*. This property is used, for example, in the BL dominated regimes in the unifying scaling theory by Grossmann & Lohse (2000, 2001).

Another classical system of thermally driven flow is horizontal convection (HC). It occurs in a fluid layer where the heating part of the layer surface is at the same horizontal level as the cooling part. Like RBC, HC is important in many geophysical systems and technology. In the large-scale ocean circulation, for instance, heat exchange between the ocean and atmosphere takes place at the ocean surface (Rossby 1965; Hughes & Griffiths 2008; Scotti & White 2011). The thermocline near the surface is of great importance in fishing and mariculture. The ground temperature in a metropolitan area is hotter than the rural area nearby, which causes significantly higher temperatures of the metropolitan air than of its surroundings. This urban heat-island effect dramatically affects global climate changes (Estrada, Botzen & Tol 2011). Horizontal convection is also relevant to engineering processes, such as glass melting and furnaces (Gramberg, Howell & Ockendon 2007; Chiu-Webster, Hinch & Liter 2008). Moreover, as it was shown recently in Wang, Lohse & Shishkina (2021), HC is closely related to internally heated convection, where the thermal driving is not due to specific thermal boundary conditions but a bulk thermal source. A number of recent theoretical, experimental and numerical studies are dedicated to the transport properties and large-scale circulation in HC under various boundary conditions (Wang & Huang 2005; Sheard & King 2011; Griffiths, Hughes & Gayen 2013; Shishkina, Grossmann & Lohse 2016; Shishkina & Wagner 2016; Wang *et al.* 2016; Passaggia *et al.* 2017*a*; Passaggia, Scotti & White 2017*b*; Shishkina 2017; Wang, Huang & Xia 2018; Ramme & Hansen 2019; Reiter & Shishkina 2020; Tsai *et al.* 2020). However, current understanding of the thermal BL structure in HC remains rather limited.

There are several major differences between the two convective systems, RBC and HC. In RBC, emission of volumes of fluid, known as ‘plumes’, rise and sink from both hot and cold BLs. They move towards the opposite plate and mix in the bulk interior, so that the BL profiles are symmetric with the respect to the bulk temperature T_o under the Boussinesq approximation. In HC, on the contrary, plumes emit from only one of the BLs and move to the other, near which the fluid starts to move back along the horizontal boundary, under the pressure gradient owing to the mean temperature difference. Such fluid motion forms

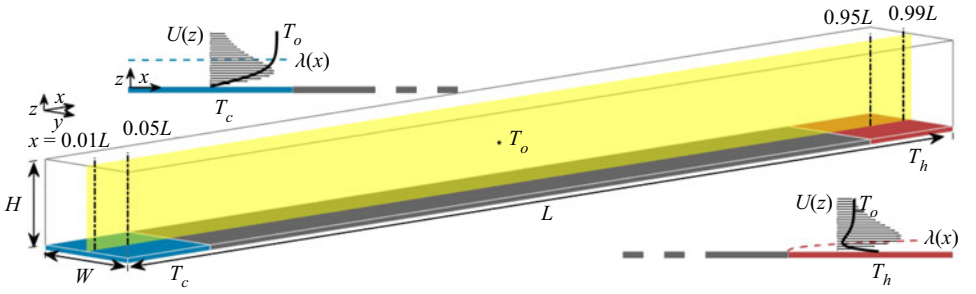

Figure 1. Schematic diagram of HC sample with the aspect ratio $L : W : H = 10 : 1 : 1$. Cooling plate (blue part) and heating plate (red part) are squares with the width W. Four vertical dashed lines indicate the locations of measured temperature profiles at $x/L = 0.01$, 0.05, 0.95 and 0.99 in the plane of $y/W = 0.5$. Also sketched are profiles of the large-scale horizontal flow and vertical mean temperature above the two plates.

a large-scale circulation that spans the whole sample. When the two BLs are separated far apart, the plumes dissipate their thermal and kinematic energies before they reach the other BL, leaving the majority of the bulk interior flow laminar except for the part near the plume-emitting BL. As a result, the HC flow is rather difficult to become turbulent compared with the RBC flow, and remains laminar in a broader Ra range. For laminar HC, the resulting bulk temperature T_o depends on the lifetime of the plumes, which is expected to be closer to the plume-emitting plate temperature as Ra increases. Therefore, the two BL profiles in HC are not symmetric with the respect to T_o and this asymmetry becomes clearer for larger Ra. Thus, the BL equations for RBC cannot be directly applied to describe the thermal BL profiles in HC.

The goal of the present work is to understand better the structures for both hot and cold thermal BLs in laminar HC and their influence on the global structure of the HC flows. We first explain in § 2 the HC experiment and the measuring procedures of mean temperature profiles near the BLs. In § 3, we propose a general thermal BL equation. We compare the experimental data with the theoretical predictions in § 4, and find good agreement between them for both BL structures. A brief summary is given in § 5.

2. Experiment

All measurements were conducted in three rectangular HC samples with the same aspect ratio $\Gamma = L : W : H = 10 : 1 : 1$, filled with water. The samples have different lengths ($L = 0.5$, 1.0 and 2.0 m) in order to extend the accessible Rayleigh number $Ra \equiv \alpha g \Delta L^3/(\nu\kappa)$ range. Here α, ν and κ denote, respectively, the isobaric thermal expansion coefficient, the kinematic viscosity and the thermal diffusivity of the fluid; g is the gravitational acceleration and $\Delta = T_h - T_c$ is the temperature difference between the heating (T_h) and cooling (T_c) plates. As shown in figure 1, both plates are squares with width W and a thickness of 5 cm, and they were placed on the sample bottom. They were made of copper and their surfaces were electroplated with a thin layer of nickel. The remaining parts of the samples were made of acrylic of 30 mm in thickness for good thermal insulation. In experiment, the samples were carefully levelled relative to gravity to within 10^{-3} rad.

The temperature difference Δ was set in the range of $10\ \text{K} \leq \Delta \leq 35\ \text{K}$ in three samples, and the corresponding Ra range is $2 \times 10^{10} \lesssim Ra \lesssim 9 \times 10^{12}$. The data show that the HC bulk temperature $T_o = T_c + \chi\Delta$ with the obtained χ from 0.81 to 0.89 over the Ra range, while $\chi = 0.5$ for RBC under the Boussinesq approximation. As a result,

the Prandtl number $Pr \equiv \nu/\kappa$, which is evaluated at T_o, varies from 3.9 to 6.5 accordingly. For $Pr \gtrsim 1$ the global heat transport in laminar HC, as expressed by the Nusselt number $Nu \equiv qL/(k\Delta)$ (q is the heat flux through the heated plate and k is the fluid thermal conductivity), is independent of Pr, while for small Pr, it scales as $Nu \sim Pr^{1/10}$ (Shishkina *et al.* 2016; Shishkina & Wagner 2016). Therefore, the variations of Pr in the experiment might lead, at most, to a 5 % error in the Nu data, which would not affect much the results on the temperature profiles. However, in order to eliminate this weak Pr dependence, we selected the measurements at $Pr \simeq 6$ only.

The procedures of temperature control and measurements in HC are similar to those in RBC described previously by He & Tong (2009). We used the calibrated thermistors (Honeywell 112-104KAJ-B01) with a diameter of 1.13 mm and accuracy of 5 mK to measure the temperature on the plates. Two thermistors were installed in each plate at a distance of 5 mm away from the top surface to ensure good thermal homogeneity. The entire HC sample was thermally insulated by several layers of rubber shields and was placed inside a temperature-controlled box. The temperature in the box was regulated at T_o with a long-time stability of ± 0.1 K, in order to prevent heat exchanges between the convection flow and the surroundings.

We used smaller glass-encapsulated thermistors (Honeywell 111-104HAK-H01) to measure time-dependent temperature profiles in the vertical z-direction, at four horizontal locations x/L above both plates, as sketched in figure 1. These thermistors have a diameter of 0.36 mm and were calibrated with 5 mK precision. We used a double-hole ceramic tube with a diameter of 0.8 mm to assemble one thermistor, and mount it on a vertical translational stage with the spatial resolution of 10 μm. Details about the temperature calibration and measurements were reported before by Wang *et al.* (2018). At each measuring location along a profile, we took 2 h-long real-time data at the rate of 15 Hz.

3. Theoretical model for laminar thermal BL in HC

For all Ra in the experiment, the maximal normalized root-mean-square (r.m.s.) temperature σ_T/Δ above the cooling plate is 0.005. In comparison, the maximal σ_T/Δ near the thermal BL in RBC for $Ra \simeq 10^9$ is approximately 0.08 (Shishkina & Thess 2009; He, Ching & Tong 2011). Recent DNS results also showed that both the kinetic energy and dissipation rate above the cooling plate are more than one decade smaller than those above the heating plate (Shishkina 2017). From these results we conclude that the turbulent fluctuations above the cooling plate are negligible, and the large-scale mean horizontal velocity U and temperature T above the cooling plate are governed by the laminar equations

$$U\partial_x U + V\partial_z U = -\rho^{-1}\partial_x P + \partial_z(\nu\partial_z U), \tag{3.1}$$

$$U\partial_x T + V\partial_z T = \partial_z(\kappa\partial_z T), \tag{3.2}$$

where ρ is the fluid density, V is the vertical mean velocity and P the hydrodynamic pressure. Such laminar HC flow can be described by a two-dimensional stream function $\Psi(x, z)$ that gives $U = \partial_z\Psi$ and $V = -\partial_x\Psi$, and can be written as

$$\Psi(x, z) = U^{max}(x)\lambda(x)\psi(\xi). \tag{3.3}$$

Here U^{max} is the maximal U which is achieved at $z = z_p$, $\lambda(x)$ is the local thermal BL thickness, $\xi = z/\lambda$ is the local similarity variable, and $\psi(\xi)$ is the universal dimensionless stream function. Previous studies (Mullarney, Griffiths & Hughes 2004; Shishkina 2017)

have shown that the z-profile of U has a single maximum. For growing z, $z > z_p$, U gradually decreases from U^{max} to 0. Thus, the boundary conditions for ψ are

$$\psi(0) = 0, \quad \psi_\xi(0) = 0, \quad \psi_\xi(\infty) = 0, \tag{3.4a–c}$$

where the subscript ξ means the derivative with respect to ξ. We denote the normalized temperature profile as

$$\theta(\xi) = (T - T_c)/(T_o - T_c), \tag{3.5}$$

and the boundary conditions for θ are

$$\theta(0) = 0, \quad \theta_\xi(0) = 1, \quad \theta(\infty) = 1. \tag{3.6a–c}$$

Substituting (3.3) and (3.5) into (3.2), one obtains the mean temperature equation:

$$\theta_{\xi\xi} + B\psi\theta_\xi = 0 \tag{3.7}$$

with $B = \lambda(U^{max}\lambda_x + U_x^{max}\lambda)/\kappa$. For laminar BL, $\lambda(x)$ follows $\lambda(x)/x \propto Re(x)^{-1/2}$ with the local Reynolds number $Re(x) = U^{max}(x)x/\nu$. From that, one has $\lambda^2(x)U^{max}(x) \propto x$ and its derivative $\lambda(2U^{max}\lambda_x + \lambda U_x^{max}) \propto x^0$. Therefore, the parameter B is a constant, independent of x.

A simple form of $\psi(\xi)$ that satisfies (3.4*a–c*) is given by

$$\psi(\xi) = \frac{c_1\xi^2}{1 + c_2^2\xi^2} \tag{3.8}$$

and its derivative is given by

$$\psi_\xi(\xi) = \frac{U(\xi)}{U^{max}} = \frac{2c_1\xi}{(1 + c_2^2\xi^2)^2}. \tag{3.9}$$

The function $\psi_\xi(\xi)$ has a maximum of 1 at $\xi = \xi_p = \sqrt{3}/(3c_2)$, leading to $c_1 = (8\sqrt{3}/9)c_2$. Substituting (3.8) into (3.7), one derives the analytical solution of the mean temperature equation:

$$\theta(\xi) = \int_0^\xi \exp\left\{-\frac{8B}{9\sqrt{3}\xi_p^2}\left[\frac{\eta}{\sqrt{3}\xi_p} - \arctan\left(\frac{\eta}{\sqrt{3}\xi_p}\right)\right]\right\} \mathrm{d}\eta. \tag{3.10}$$

Here B is chosen to satisfy $\theta(\infty) = 1$, and $\xi_p = z_p/\lambda = \sqrt{3}/(3c_2)$. Both, z_p and λ, are expected to depend on x, so does their ratio ξ_p. When $\xi_p \to \infty$, i.e. the thermal BL is nested infinitely deep within the linear part of $U(\xi)$, the temperature profile tends to the PBP profile for infinite Pr. Note that for large Pr (and this is also the considered case of water), the thermal BL is nested in the viscous one and therefore the choice of the stream function form (e.g. as in (3.8)) is quite flexible and not that influential on the accuracy of the temperature profiles predictions, as soon as the boundary conditions (3.4*a–c*) are fulfilled and the stream function form allows flexibility for z_p.

4. Experimental results

Figure 2(*a*) shows a typical example of a mean (time-averaged) temperature profile T as a function of z above the cooling plate ($x/L = 0.01$ and 0.05) and above the heating plate ($x/L = 0.95$ and 0.99) at a half-width ($y/W = 0.5$) for $Ra = 3.57 \times 10^{12}$. We determine

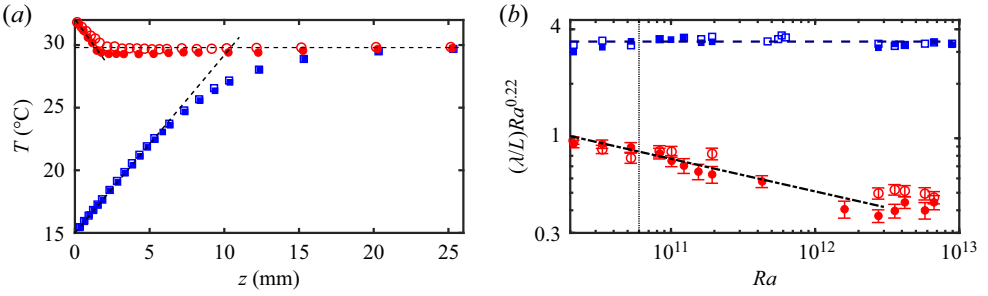

Figure 2. (*a*) Measured time-averaged temperature T as a function of z, for $Ra = 3.57 \times 10^{12}$. Two short dashed lines are tangents of T near the plates for $x/L = 0.05$ and 0.95. The long horizontal dashed line indicates $T_o = 29.8\,^{\circ}\mathrm{C}$ at the sample centre. (*b*) Reduced thermal BL thickness $(\lambda/L)\,Ra^{0.22}$ as a function of Ra for varying x/L. Dashed line represents the power function $\lambda/L = 3.42\,Ra^{-0.22}$. Vertical dotted line is placed at $Ra = 6 \times 10^{10}$. Dotted-dashed line represents the power function $\lambda/L = 73.5\,Ra^{-0.40}$. In panels (*a*,*b*), blue solid (open) squares are for $x/L = 0.01$ (0.05), and red solid (open) circles for $x/L = 0.95$ (0.99).

the local thermal BL thickness λ by the intersection of the tangent of T for $z \simeq 0$ and the bulk temperature T_o for large z. It is found that the thermal BL above the cooling plate is much thicker than that above the heating plate, indicating different structures of the cold and hot thermal BLs.

Figure 2(*b*) shows the Ra dependence of λ/L measured at the four locations. The two sets of data above the cooling plate are nearly the same, and they both follow the power-law scaling $\lambda/L = 3.42\,Ra^{-0.22}$ over the studied Ra range. For simplicity, we use $\lambda_c = \lambda(x/L = 0.05)$ to denote the cold thermal BL thickness. In contrast to the data for the cooling plate, the two datasets above the heating plate are close but do not follow the universal scaling with Ra. We use $\lambda_h = \lambda(x/L = 0.95)$ to denote the hot thermal BL thickness. The ratio of λ_h to λ_c has a maximum of 0.28 at the lowest $Ra = 2 \times 10^{10}$, and it decreases down to around 0.1 as Ra increases above 10^{12}.

In figure 3, we show the normalized profiles $(T - T_c)/(T_o - T_c)$ as function of z/λ_c measured at $x/L = 0.01$ and 0.05 for different Ra. It is found that the two sets of data collapse and agree well with the θ-profile predicted by (3.10) with $\xi_p = 0.44$. It indicates that our model captures essential physics behind the cold thermal BL structure. The value of ξ_p indicates that the location of U^{max} is at $z_p = 0.44\lambda_c$, inside the cold thermal BL. When z_p is far outside the thermal BL (for instance $\xi_p = 5$), the θ predicted by (3.10) tends to the PBP temperature profile for $Pr \to \infty$, as illustrated in the inset of figure 3.

Figure 4(*a*) shows the normalized profiles $(T_h - T)/(T_h - T_o)$ measured at $x = 0.95L$ for varying Ra and $Pr \simeq 6$. For $z < \lambda_h$, the Nusselt number can be approximately expressed by $Nu = (L/\Delta)(\partial T/\partial z)|_{z<\lambda_h}$. Recent DNS results (Reiter & Shishkina 2020) revealed that the heat transport dynamics undergoes several transitions from steady state to chaotic state as Ra increases. For $Pr = 10$, the $Nu(t)$ data start to oscillate at $Ra \simeq 3 \times 10^{10}$ and transit to a chaotic state at $Ra \simeq 5 \times 10^{11}$. The multiple states of Nu dynamics have different effects on the thermal BL structure above the heating plate. Consequently, the normalized profiles near the thermal BL do not have a universal scaling over the studied Ra range. With the same data as in figure 4(*a*), we plot $(T - T_c)/(T_o - T_c)$ as a function of z/λ_c in figure 4(*b*). It is found that for large z, the data collapse onto a single master curve. As z decreases while moving from the bulk towards the plate, T decreases from T_o to a minimal value, in a similar way as that near the cold thermal BL. When z is further down to the heating plate, T starts to increase as it is heated by the hot thermal BL. At

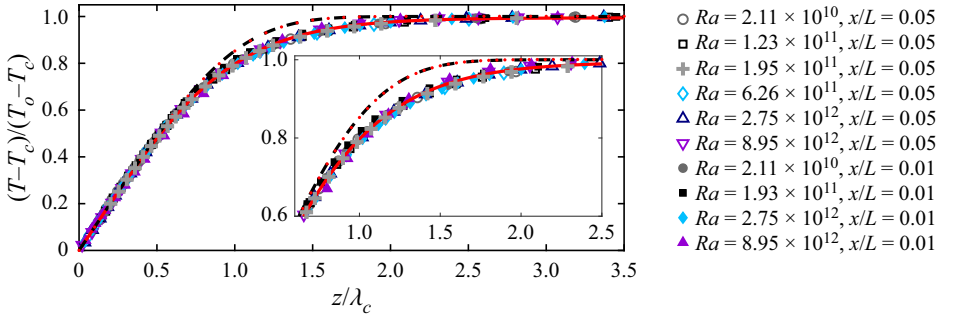

Figure 3. Normalized mean temperature $(T - T_c)/(T_o - T_c)$ as a function of z/λ_c for varying Ra. Crosses are for $Pr = 3.9$ and other symbols for $Pr \simeq 6$. The measurements were made above the cooling plate at $x/L = 0.01$ and 0.05. The red solid (dotted) line represents (3.10) with $\xi_p = 0.44$ (5). The black dashed line shows the PBP temperature profile for $Pr \to \infty$. Inset shows an enlarged view.

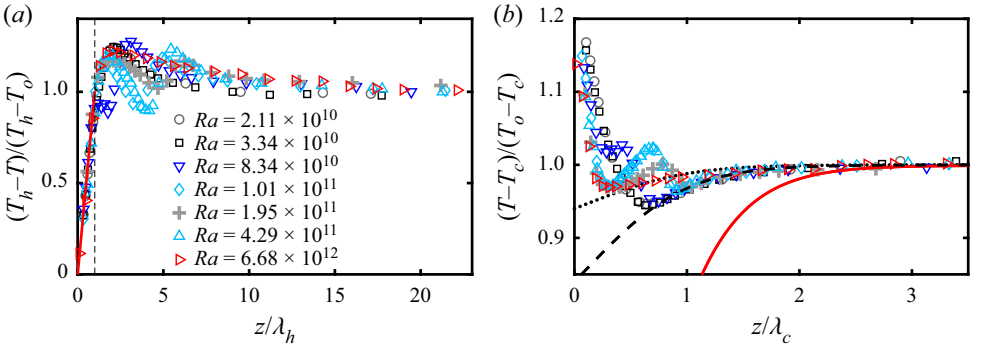

Figure 4. (*a*) Measured $(T_h - T(z))/(T_h - T_o)$ as a function of z/λ_h at $x/L = 0.95$ for varying Ra. Crosses are for $Pr = 3.9$ and other symbols for $Pr \simeq 6$. The red solid line is a linear function. (*b*) Measured $(T(z) - T_c)/(T_o - T_c)$ as a function of z/λ_c. The data are the same as in panel (*a*). The red solid line represents (3.10) with $\xi_p = 0.44$. The black dashed (dotted) line represents (4.2) with $\xi_p = 0.44$ and $a/\chi = 0.84$ (0.94).

$z = 0$, the normalized profile has the amplitude of $\chi \equiv (T_o - T_c)/(T_h - T_c)$. Different χ values clearly show that the normalized temperature data no longer overlap.

Figure 4 thus reveals that the thermal flow above the heating plate can be divided into two regions: a hot lower region with $T \gtrsim T_o$, where the normalized temperature scales with λ_h, and a cold upper one with $T(z) \lesssim T_o$, where the normalized temperature scales with λ_c and follows the predicted shape (3.10). The separation between the two length scales, λ_h and λ_c, increases as Ra increases, therefore the normalized T cannot scale as either one of them over the two regions. For the cold region, we define a reference temperature $T_c^* = T_c + a\Delta$ $(0 \le a \le \chi)$ so that T between T_c^* and T_o follows the predicted scaling for

$$\theta(z/\lambda_c) \equiv (T - T_c^*)/(T_o - T_c^*). \tag{4.1}$$

Then we have

$$\frac{T - T_c}{T_o - T_c} = \theta(z/\lambda_c) + \frac{a}{\chi}\left[1 - \theta(z/\lambda_c)\right]. \tag{4.2}$$

As shown in figure 4(*b*), the overlapped profiles in the cold region can be well described by (4.2) with $\xi_p = 0.44$ and $a = 0.84\chi$, both independent of Ra. However, the obtained χ

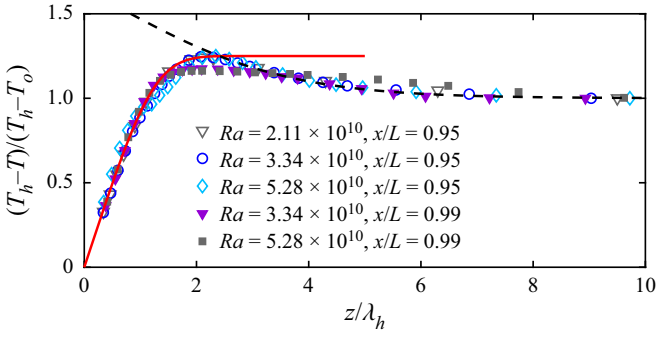

Figure 5. Measured $(T_h - T)/(T_h - T_o)$ as a function of z/λ_h, measured at $x/L = 0.95$ and 0.99 for varying Ra. For these measurements, $\chi = 0.82$. The black dashed line represents (4.1) with $\xi_p = 0.44$ and $a = 0.69$. The red solid line is (4.5) with $\xi_p = 1.6$ and $b = 0.77$.

increases with Ra from 0.81 to 0.89 (the bulk becomes hotter with increasing Ra) over the range $2 \times 10^{10} \lesssim Ra \lesssim 9 \times 10^{12}$.

Similar to the cold region, the temperature profiles in the hot region are expected to follow the predicted θ-form over the range from T_h to a reference temperature $T_h^* = T_c + b\Delta$ $(0 \le b \le \chi)$ for

$$\theta(z/\lambda_h^*) \equiv (T_h - T)/(T_h - T_h^*), \tag{4.3}$$

where $\lambda_h^* \ge \lambda_h$ is the effective hot thermal BL thickness that accounts for the excessive temperature drop $T_o - T_h^*$. For laminar BL, one has

$$\frac{\lambda_h^*}{\lambda_h} = \frac{T_h - T_h^*}{T_h - T_o} = \frac{1-b}{1-\chi}. \tag{4.4}$$

From (4.3) and (4.4), the dimensionless mean temperature equation for the hot region can be written as

$$\frac{T_h - T(z)}{T_h - T_o} = \frac{1-b}{1-\chi}\theta(z/\lambda_h^*). \tag{4.5}$$

Since θ has a maximum of 1, the value of b is determined by the minimal value of T from the measurements.

In figure 5, we show $(T_h - T)/(T_h - T_o)$ as a function of z/λ_h, measured at $x/L = 0.95$ and 0.99 above the heating plate. We choose the data for $Ra \lesssim 6 \times 10^{10}$ in order to exclude the Nu oscillation effects on the BL structures, and we take the averaged $\chi = 0.82$ over the Ra range. It is found that the three dimensionless profiles for $x/L = 0.95$ scale with λ_h for $z/\lambda_h \lesssim 2.2$, and they are well described by (4.5) with $\xi_p = 1.6$ and $b = 0.77$. In the cold region, the three profiles almost overlap as well, since the ratio of λ_c/λ_h is nearly constant ≈ 0.28 for these values of Ra.

The black dashed line in figure 5 represents the same calculated T-values as those in figure 4(*b*), but re-scaled in a different dimensionless form. The ratio of $\xi_p = 1.6$ for the hot region to $\xi_p = 0.44$ for the cold region is consistent with the ratio of λ_c/λ_h. Note that for $x/L = 0.95$ the two fitting ranges intersect at the same temperature. It indicates that the hot and cold regions are nearly adjacent to each other, which forms a double-BL structure above the heating plate. At $x/L = 0.99$ near the vertical sidewall, the normalized T-data are almost constant around $z/\lambda_h = 2.2$, close to the interface between the two regions. It may be caused by the mixing of uprising thermal plumes. As Ra increases, both the mixing

intensity and the separation of the two scales increase. Above a certain Ra, (for instance, when $Ra \simeq 10^{12}$, $\lambda_c/\lambda_h = 10$), the double-BL structure is expected to be highly unstable and HC eventually transits to a chaotic state.

5. Summary

We presented experimental results for the time-averaged vertical temperature profiles θ near the thermal BLs at the bottom of HC samples over the range $2 \times 10^{10} \lesssim Ra \lesssim 9 \times 10^{12}$ and for $Pr \simeq 6$ and demonstrated that the profiles scale with the thicknesses λ_c and λ_h of, respectively, cold and hot thermal BLs. Near the cold thermal BL, all temperature profiles have a universal scaling form $\theta(z/\lambda_c)$ for $0 \lesssim z/\lambda_c \lesssim 3.5$. Under assumption of a single maximum in the vertical profile of the large-scale horizontal velocity U near the BL, we derived (3.10) for $\theta(z/\lambda_c)$ that can well describe the collapsing experimental $\theta(z/\lambda_c)$ profiles.

The θ-profile above the heating plate has, however, a more complicated structure, which can be split into two regions. In the hot region below, the θ data scale with the similarity variable z/λ_h, while in the cold region above, they scale with z/λ_c. In both regions, the shapes of the profiles are in good agreement with the predicted form (3.10) for laminar BL. The result thus reveals a double-layer structure for the temperature field above the heated plate. For $Ra \lesssim 6 \times 10^{10}$, the scaling ranges of the two regions nearly coincide, which indicates that the entire hot thermal BL is laminar. As Ra increases, the increasing scale separation allows fluctuations in the hot region. In the range $10^{11} \lesssim Ra \lesssim 4.3 \times 10^{11}$, local θ-profiles have spatial oscillations for $\lambda_h \lesssim z \lesssim \lambda_c$. Above $Ra \simeq 10^{12}$, at which $\lambda_c/\lambda_h \simeq 10$, there are more fluctuations in the hot region that render the shape of θ further different from what can be predicted with the laminar BL equation. The profiles in the cold region, however, still follow the laminar equation. This suggests that the rest of the HC flow remains to be rather laminar. The change of the scaling form $\theta(z/\lambda_h)$ in the hot region with growing Ra is consistent with the change of the Nu dependence on Ra observed by Reiter & Shishkina (2020).

Acknowledgements. We are very grateful to P. Tong and E. Ching for many insightful discussions.

Funding. X.H. acknowledges support of the National Natural Science Foundation of China (grant nos 11772111 and 91952101), the Science and Technology Innovation Commission of Shenzhen (no. KQJSCX20180328165817), and of Max Planck Partner Group. O.S. acknowledges support of the Deutsche Forschungsgemeinschaft (DFG) under grant Sh405/10.

Declaration of interests. The authors report no conflict of interest.

Author ORCIDs.
Bo Yan https://orcid.org/0000-0003-1384-0589;
Olga Shishkina https://orcid.org/0000-0002-6773-6464;
Xiaozhou He https://orcid.org/0000-0001-8116-889X.

References

Ahlers, G., Grossmann, S. & Lohse, D. 2009 Heat transfer and large scale dynamics in turbulent Rayleigh–Bénard convection. *Rev. Mod. Phys.* **81**, 503–538.

Ching, E.S.C., Dung, O.-Y. & Shishkina, O. 2017 Fluctuating thermal boundary layers and heat transfer in turbulent Rayleigh–Bénard convection. *J. Stat. Phys.* **167**, 626–635.

Ching, E.S.C., Leung, H.S., Zwirner, L. & Shishkina, O. 2019 Velocity and thermal boundary layer equations for turbulent Rayleigh–Bénard convection. *Phys. Rev. Res.* **1**, 033037.

Chiu-Webster, S., Hinch, E.J. & Liter, J.R. 2008 Very viscous horizontal convection. *J. Fluid Mech.* **611**, 395–426.

ESTRADA, F., BOTZEN, W.J.W. & TOL, R.S.J. 2011 A global economic assessment of city policies to reduce climate change impacts. *Nat. Clim. Change* **23**, 025106.

GRAMBERG, H.J.J., HOWELL, P.D. & OCKENDON, J.R. 2007 Convection by a horizontal thermal gradient. *J. Fluid Mech.* **586**, 41–57.

GRIFFITHS, R.W., HUGHES, G.O. & GAYEN, B. 2013 Horizontal convection dynamics: insights from transient adjustment. *J. Fluid Mech.* **76**, 559–595.

GROSSMANN, S. & LOHSE, D. 2000 Scaling in thermal convection: a unifying theory. *J. Fluid Mech.* **407**, 27–56.

GROSSMANN, S. & LOHSE, D. 2001 Thermal convection for large Prandtl numbers. *Phys. Rev. Lett.* **86**, 3316–3319.

GROSSMANN, S. & LOHSE, D. 2011 Multiple scaling in the ultimate regime of thermal convection. *Phys. Fluids* **23**, 045108.

HE, X., BODENSCHATZ, E. & AHLERS, G. 2021 A model for universal spatial variations of temperature fluctuations in turbulent Rayleigh–Bénard convection. *Theor. Appl. Mech. Lett.* **11**, 1.

HE, X., CHING, E.S.C. & TONG, P. 2011 Locally-averaged thermal dissipation rate in turbulent thermal convection: a decomposition into contributions from different temperature gradient components. *Phys. Fluids* **23**, 025106.

HE, X. & TONG, P. 2009 Measurements of the thermal dissipation field in turbulent Rayleigh–Bénard convection. *Phys. Rev.* E **79**, 026306.

HUGHES, G.O. & GRIFFITHS, R.W. 2008 Horizontal convection. *Annu. Rev. Fluid Mech.* **40** (1), 185–208.

KRAICHNAN, R.H. 1962 Turbulent thermal convection at arbritrary Prandtl number. *Phys. Fluids* **5**, 1374–1389.

MULLARNEY, J.C., GRIFFITHS, R.W. & HUGHES, G.O. 2004 Convection driven by differential heating at a horizontal boundary. *J. Fluid Mech.* **516**, 181–209.

PASSAGGIA, P.-Y., HURLEY, M.W., WHITE, B. & SCOTTI, A. 2017*a* Turbulent horizontal convection at high Schmidt numbers. *Phys. Rev. Fluids* **2**, 090506.

PASSAGGIA, P.-Y., SCOTTI, A. & WHITE, B. 2017*b* Transition and turbulence in horizontal convection: linear stability analysis. *J. Fluid Mech.* **821**, 31–58.

RAMME, L. & HANSEN, U. 2019 Transition to time-dependent flow in highly viscous horizontal convection. *Phys. Rev. Fluids* **4**, 093501.

REITER, P. & SHISHKINA, O. 2020 Classical and symmetrical horizontal convection: detaching plumes and oscillations. *J. Fluid Mech.* **892**, R1.

ROSSBY, H.T. 1965 On thermal convection driven by non-uniform heating from below: an experimental study. *Deep Sea Res.* **12**, 9–16.

SCHLICHTING, H. & GERSTEN, K. 2000 *Boundary Layer Theory*, 8th edn. Springer.

SCOTTI, A. & WHITE, B. 2011 Is horizontal convection really 'non-turbulent?' *Geophys. Res. Lett.* **38**, L21609.

SHEARD, G.J. & KING, M.P. 2011 Horizontal convection: effect of aspect ratio on Rayleigh number scaling and stability. *Appl. Math. Model.* **35**, 1647–1655.

SHISHKINA, O. 2017 Mean flow structure in horizontal convection. *J. Fluid Mech.* **812**, 525–540.

SHISHKINA, O., GROSSMANN, S. & LOHSE, D. 2016 Heat and momentum transport scalings in horizontal convection. *Geophys. Res. Lett.* **43** (3), 1219–1225.

SHISHKINA, O., HORN, S., EMRAN, M.S. & CHING, E.S.C. 2017 Mean temperature profiles in turbulent thermal convection. *Phys. Rev. Fluids* **2**, 113502.

SHISHKINA, O., HORN, S., WAGNER, S. & CHING, E.S.C. 2015 Thermal boundary layer equation for turbulent Rayleigh–Bénard convection. *Phys. Rev. Lett.* **114**, 114302.

SHISHKINA, O. & THESS, A. 2009 Mean temperature profiles in turbulent Rayleigh–Bénard convection of water. *J. Fluid Mech.* **633**, 449–460.

SHISHKINA, O. & WAGNER, S. 2016 Prandtl-number dependence of heat transport in laminar horizontal convection. *Phys. Rev. Lett.* **116**, 024302.

SHRAIMAN, B.I. & SIGGIA, E.D. 1990 Heat transport in high-Rayleigh number convection. *Phys. Rev.* A **42**, 3650–3653.

SPIEGEL, E.A. 1971 Convection in stars. *Annu. Rev. Astron. Astrophys.* **9**, 323–352.

TSAI, T., HUSSAM, W.K., KING, M.P. & SHEARD, G.J. 2020 Transitions and scaling in horizontal convection driven by different temperature profiles. *Intl J. Therm. Sci.* **148**, 106166.

WANG, F., HUANG, S. & XIA, K. 2018 Contribution of surface thermal forcing to mixing in the ocean. *J. Geophys. Res.* **123** (2), 855–863.

WANG, F., HUANG, S., ZHOU, S. & XIA, K. 2016 Laboratory simulation of the geothermal heating effects on ocean overturning circulation. *J. Geophys. Res.* **121** (10), 7589–7598.

WANG, Q., LOHSE, D. & SHISHKINA, O. 2021 Scaling in internally heated convection: a unifying theory. *Geophys. Res. Lett.* **48**, e2020GL091198.

WANG, W. & HUANG, R.X. 2005 An experimental study on thermal circulation driven by horizontal differential heating. *J. Fluid Mech.* **540**, 49–73.

WANG, Y., HE, X. & TONG, P. 2016 Boundary layer fluctuations and their effects on mean and variance temperature profiles in turbulent Rayleigh–Bénard convection. *Phys. Rev. Fluids* **1**, 082301(R).

WANG, Y., XU, W., HE, X., YIK, H., WANG, X., SCHUMACHER, J. & TONG, P. 2018 Boundary layer fluctuations in turbulent Rayleigh–Bénard convection. *J. Fluid Mech.* **840**, 408–431.

XU, W., WANG, Y., HE, X., WANG, X., SCHUMACHER, J., HUANG, S. & TONG, P. 2021 Mean velocity and temperature profiles in turbulent Rayleigh–Bénard convection at low Prandtl numbers. *J. Fluid Mech.* (in press).